

Internal Tide Generation Using Green Function Analysis: To WKB or Not to WKB?

MANIKANDAN MATHUR

Department of Aerospace Engineering, Indian Institute of Technology Madras, Chennai, India

GLENN S. CARTER

Department of Oceanography, University of Hawai'i at Mānoa, Honolulu, Hawaii

THOMAS PEACOCK

Department of Mechanical Engineering, Massachusetts Institute of Technology, Cambridge, Massachusetts

(Manuscript received 5 August 2015, in final form 14 March 2016)

ABSTRACT

An established analytical technique for modeling internal tide generation by barotropic flow over bottom topography in the ocean is the Green function–based approach. To date, however, for realistic ocean studies this method has relied on the WKB approximation. In this paper, the complete Green function method, without the WKB approximation, is developed and tested, and in the process, the accuracy of the WKB approximation for realistic ridge geometries and ocean stratifications is considered. For isolated Gaussian topography, the complete Green function approach is shown to be accurate via close agreement with the results of numerical simulations for a wide range of height ratios and criticality; in contrast, the WKB approach is found to be inaccurate for small height ratios in the subcritical regime and all tall topography that impinges on the pycnocline. Two ocean systems are studied, the Kaena and Wyville Thomson Ridges, for which there is again excellent agreement between the complete Green function approach and numerical simulations, and the WKB approximate solutions have substantial errors. This study concludes that the complete Green function approach, which is typically only modestly more computationally expensive than the WKB approach, should be the go-to analytical method to model internal tide generation for realistic ocean ridge scenarios.

1. Introduction

The generation of baroclinic (internal) tides via barotropic tidal flow over topography is a principal source of mechanical energy that ultimately drives ocean interior mixing (Munk and Wunsch 1998). As such, several different analytical and numerical models have been developed to investigate this process (e.g., Bell 1975; Baines 1982; Holloway and Merrifield 1999; Balmforth et al. 2002; Zarroug et al. 2010). These models have contributed significantly to the current understanding of

internal tide generation, and practically they provide reasonable quantitative estimates of the rate of barotropic-to-baroclinic tidal conversion for many important ocean settings.

A popular analytical model of internal tide generation is a Green function–based approach that was initially developed to study internal tide scattering by two-dimensional, knife-edge topography in a uniformly stratified fluid (Robinson 1969). Llewellyn-Smith and Young (2002) employed Green functions to estimate the barotropic-to-baroclinic conversion rate at weak, three-dimensional topography in a nonuniformly stratified, finite-depth ocean in the limit of hydrostatic waves and subcritical topography, invoking the WKB approximation, which assumes a vertically varying, local vertical wavenumber for the internal wave field and requires

Corresponding author address: Manikandan Mathur, Department of Aerospace Engineering, Indian Institute of Technology Madras, Guindy, Chennai 600036, India.
E-mail: manims@ae.iitm.ac.in

variations in the stratification to occur on significantly larger scales than the local vertical wavelength. It was [Llewellyn-Smith and Young \(2003\)](#), however, who directly extended the approach of [Robinson \(1969\)](#) to analytically calculate conversion rates for barotropic tidal flow past a finite-height, two-dimensional, knife-edge barrier in a finite-depth ocean, again in the limit of the WKB approximation. Thereafter, [Pétrélis et al. \(2006\)](#) adapted the approach for finite-height, two-dimensional topographies of any symmetric shape in a uniformly stratified, finite-depth ocean. [Balmforth and Peacock \(2009\)](#) modified the approach for studies of periodic supercritical topography in a uniformly stratified ocean of infinite depth, and [Echeverri and Peacock \(2010\)](#) advanced the Green function approach to handle two-dimensional topographies of arbitrary shape in a finite-depth ocean of arbitrary stratification, albeit assuming the WKB approximation. Most recently, [Falahat et al. \(2014\)](#) performed global linear computations of tidal energy conversion by small-amplitude, subcritical topography without the WKB approximation, comparing how the accuracy depends on the topographic length scale.

In this paper, we further advance the Green function method to enable the study of internal tide generation by arbitrary, two-dimensional topography in arbitrary nonuniform stratifications without the restriction of the WKB approximation. The analytical method and corresponding WKB approximations are presented in [section 2](#), followed by a brief description of our supporting numerical model in [section 3](#). In [section 4](#), we consider isolated Gaussian topographies in a non-uniform stratification and investigate the shortcomings of WKB-based predictions. We then apply the method to two realistic scenarios in [section 5](#), considering transects from two very different ocean ridge systems with very different background stratifications, again comparing the results to those of WKB-based predictions. In all cases, our results are validated by comparisons with the results of the numerical model described in [section 3](#). Finally, in [section 6](#), we present our conclusions.

2. Theory

We define a streamfunction $\psi(x, z, t)$ so that the associated velocity field is $(u, w) = (-\psi_z, \psi_x)$, with x and z as the horizontal and vertical coordinates, respectively. The streamfunction of the total wave field is $\psi(x, z, t) = \psi_b(x, z, t) + \psi'(x, z, t)$, where $\psi_b = \text{Re}(-Uze^{-i\omega t})$ represents the background barotropic forcing of velocity amplitude U , and ψ' is the internal wave field generated by the barotropic forcing. It is assumed that the response

is at the same frequency ω as the barotropic tide, that is, $\psi_b = \text{Re}[\phi_b(x, z)e^{-i\omega t}]$ and $\psi' = \text{Re}[\phi'(x, z)e^{-i\omega t}]$, where t is time, ϕ_b and ϕ' are complex amplitudes, and Re denotes the real part.

The perturbation streamfunction $\phi'(x, z)$ satisfies the inviscid linear internal wave equation under the Boussinesq approximation ([Balmforth et al. 2002](#)):

$$\left[\frac{N(z)^2 - \omega^2}{\omega^2 - f^2} \right] \phi'_{xx} - \phi'_{zz} = 0, \quad (1)$$

where $N(z)$ is the background stratification, and f is the constant Coriolis frequency. No normal flow at the ocean floor topography $h(x)$ and the sea surface (approximated as a rigid lid) require

$$\phi'[x, h(x)] = Uh(x) \quad \text{and} \quad \phi'(x, H) = 0, \quad (2)$$

where H is the far-field ocean depth. The bottom topography $z = h(x) \geq 0$ is any continuous function going smoothly to zero at $x = -a$ and $x = b$, and $z = 0$ for $x \notin [-a, b]$, corresponding to a flat ocean bottom.

Following the approaches of [Robinson \(1969\)](#), [Pétrélis et al. \(2006\)](#), [Balmforth and Peacock \(2009\)](#), and [Echeverri and Peacock \(2010\)](#), we write the solution to (1)–(2) as a summation over a distribution of sources of strength $\gamma(x')$ distributed over the topography, that is,

$$\phi'(x, z) = \int_{-a}^b \gamma(x') G[x, x'; z, h(x')] dx', \quad (3)$$

where $G(x, x'; z, z')$ is the Green function that satisfies the equation

$$\left[\frac{N(z)^2 - \omega^2}{\omega^2 - f^2} \right] G_{xx} - G_{zz} = i\delta(x - x')\delta(z - z'), \quad (4)$$

subject to the homogeneous boundary conditions $G(x, x'; 0, z') = G(x, x'; H, z') = 0$, where $\delta(x)$ is the delta function. Based on a standard procedure ([Robinson 1969](#); [Pétrélis et al. 2006](#); [Echeverri and Peacock 2010](#)), one can show that the Green function that satisfies the aforementioned boundary conditions [plus the radiation condition that requires disturbances to propagate away from a source at (x', z')] is given by

$$G(x, x'; z, z') = \sum_{n=1}^{n=\infty} \frac{\Phi_n(z')}{2k_n \Gamma_n} e^{ik_n|x-x'|} \Phi_n(z), \quad (5)$$

where Φ_n is the n th vertical mode, satisfying

$$\Phi_{n,zz} + \frac{N(z)^2 - \omega^2}{\omega^2 - f^2} k_n^2 \Phi_n = 0, \quad (6)$$

with homogeneous boundary conditions $\Phi_n(0) = \Phi_n(H) = 0$, and the positive eigenvalue k_n is the corresponding horizontal wavenumber. The factor Γ_n is given by

$$\Gamma_n = \int_0^H \frac{N(z)^2 - \omega^2}{\omega^2 - f^2} \Phi_n^2 dz. \quad (7)$$

Prior to the present study, all internal tide generation studies using this theoretical formulation for nonuniform stratifications have computed the Green function either for a uniform stratification or under the WKB approximation for a nonuniform stratification, and the complete formulation involving (5) and (6) has not been utilized. We also note that the hydrostatic approximation is not invoked in (4) or any of the subsequent expressions.

Equation (6), with the homogeneous boundary conditions, constitutes a Sturm–Liouville system that must be solved numerically to obtain Φ_n for an arbitrary stratification $N(z)$. For convenience, and without any loss of generality, we define Φ_n such that $\int_0^H [\Phi_n(z)]^2 dz = 1$. Using the complete Green function (CGF) approach, that is, the numerical solutions of (6), the expression for the perturbation streamfunction in an arbitrary stratification is

$$\phi'(x, z) = \sum_{n=1}^{n=\infty} \frac{1}{2k_n \Gamma_n} \Phi_n(z) \int_{-a}^b \gamma(x') \Phi_n[h(x')] e^{ik_n|x-x'|} dx', \quad (8)$$

where $\gamma(x')$, being the distribution of point sources, is the quantity to be solved for by imposing the boundary condition at the bottom topography in (2).

The first boundary condition in (2) now results in the integral equation

$$Uh(x) = \phi'[x, h(x)] = \sum_{n=1}^{n=\infty} \frac{1}{2k_n \Gamma_n} \Phi_n[h(x)] \int_{-a}^b \gamma(x') \Phi_n[h(x')] e^{ik_n|x-x'|} dx', \quad (9)$$

which is solved numerically for $\gamma(x')$ using the procedure detailed in Echeverri and Peacock (2010). In solving this numerically, one must use a sufficiently fine resolution to represent the topography and a sufficiently large number of modes in the summation so that the solution converges. In section 4, for example, the Gaussian topographies were discretized using 1081 points ($-2.7\sigma_G \leq x \leq 2.7\sigma_G$, σ_G being the $(1/e)$ -width of the topography), and a maximum of 600 modes were used in the summation, with the shorter topographies requiring a larger number of modes than their taller counterparts. The results presented in section 5 for realistic topography were obtained using 200 modes,

with a horizontal grid size of 50 and 30 m to represent the topography at the Kaena Ridge and Wyville Thomson Ridge, respectively.

In the far field, where the ocean depth is constant, one can define

$$a_n^\pm = \frac{1}{2k_n \Gamma_n} \int_{-a}^b \gamma(x') \Phi_n[h(x')] e^{\mp ik_n x'} dx', \quad (10)$$

where a_n^+ corresponds to $x > b$ and a_n^- to $x < -a$. The far-field perturbation streamfunction can thus be written explicitly and concisely as a sum over the vertical modes:

$$\phi'(x, z) = \sum_{n=1}^{n=\infty} a_n^\pm \Phi_n(z) e^{\pm ik_n x}. \quad (11)$$

The total wave field is given by $\phi(x, z) = \phi_b + \phi'$, in which case the cumulative right-propagating (+) and left-propagating (−) time-averaged and depth-integrated energy fluxes in mode p through mode q are

$$E_{p-q}^\pm = \sum_{n=p}^{n=q} E_n^\pm = \sum_{n=p}^{n=q} \frac{\rho_0 \omega}{2} \frac{\omega^2 - f^2}{\omega^2} \frac{|a_n^\pm|^2}{k_n} \int_0^H \left(\frac{d\Phi_n}{dz} \right)^2 dz, \quad (12)$$

where ρ_0 is a reference background density. The total right- and left-propagating energy fluxes are denoted by E^+ and E^- , respectively, where $E^\pm = \sum_{n=1}^{n=\infty} E_n^\pm$ with dimensions of power per unit distance in the y direction.

In the WKB approximation, the mode shapes $\Phi_n(z)$ and the horizontal wavenumbers k_n in (8)–(11) are replaced by the WKB mode shapes $\Phi_{n,\text{wkb}}(z)$ and their corresponding horizontal wavenumbers (Llewellyn-Smith and Young 2003; Echeverri and Peacock 2010). The WKB eigenfunctions are

$$\Phi_{n,\text{wkb}}(z) = \frac{1}{M_n} \frac{\sin[nZ(z)]}{\sqrt{\mathcal{N}}}, \quad (13)$$

where

$$Z(z) = \frac{\pi}{HN_m} \int_0^z \sqrt{N(z_1)^2 - \omega^2} dz_1, \quad (14)$$

$$N_m = \frac{1}{H} \int_0^H \sqrt{N(z)^2 - \omega^2} dz, \quad (15)$$

$$\mathcal{N}(z) = \frac{1}{N_m} \sqrt{N(z)^2 - \omega^2}, \quad \text{and} \quad (16)$$

$$M_n = \sqrt{\int_0^H \frac{\sin^2[nZ(z)]}{\mathcal{N}} dz}. \quad (17)$$

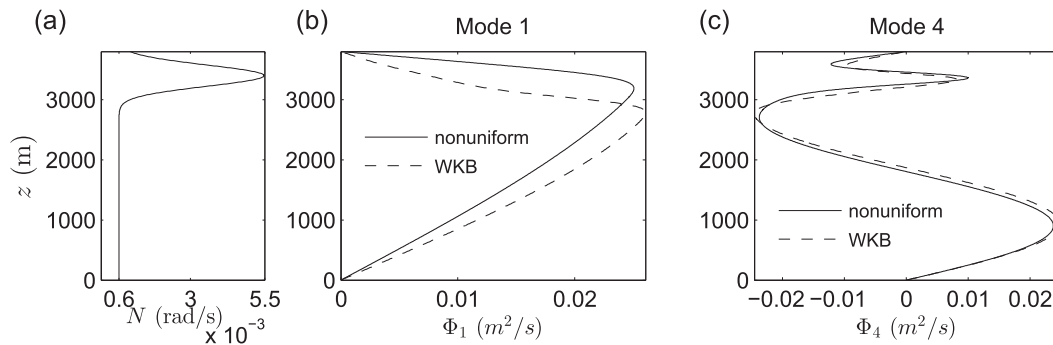


FIG. 1. (a) The stratification profile $N(z)$ considered in section 4. The streamfunction $\Phi(z)$ for (b) mode 1 and (c) mode 4 for the stratification in (a), as determined by solving (6) numerically (solid line) and by using the WKB approximation (dashed line). The streamfunctions are normalized so that $\int_0^H \Phi^2 dz = 1$.

The corresponding eigenvalues are $k_n = n\pi/\mu H$, where $\mu = N_m/\sqrt{\omega^2 - f^2}$. If the WKB mode strengths are denoted by $a_{n,\text{wkb}}^\pm$, the energy fluxes are given by

$$E_{p-q,\text{wkb}}^\pm = \sum_{n=p}^{n=q} E_{n,\text{wkb}}^\pm = \frac{\pi\rho_0 N_m^2}{4\mu\omega} \sum_{n=p}^{n=q} n \frac{|a_{n,\text{wkb}}^\pm|^2}{M_n^2}. \quad (18)$$

3. Numerics

To validate the solutions obtained using the complete Green function approach and further confirm the errors associated with the WKB approach, we ran several corresponding numerical simulations based on the nonlinear, hydrostatic, terrain-following (σ coordinate) Princeton Ocean Model (Blumberg and Mellor 1987). Simulations were conducted in a narrow channel with the topography of interest in the center of the domain and periodic boundary conditions in the across-channel direction, which is equivalent to a 2D x - z domain (results are constant with y). The Princeton Ocean Model uses a Mellor–Yamada turbulence closure scheme (Mellor and Yamada 1982; Blumberg and Mellor 1987) in the vertical. Although it is possible to add a background diffusivity level, this was not applied here. In the horizontal, the model uses a Smagorinsky diffusivity (Smagorinsky 1963; Blumberg and Mellor 1987), which is set to zero in our simulations (and hence no explicit horizontal diffusivity is applied). However, as with all numerical models, there is numerical diffusion.

Modal decomposition was performed over the flat bottom sections upstream and downstream of the topographic feature. The boundary forcing at the ends of the channel was through the Flather condition (Flather 1976; Carter and Merrifield 2007) with the surface elevation chosen to correspond to an along-channel velocity of $U = 2.5 \times 10^{-4} \text{ m s}^{-1}$. At the ends of the channel the relaxation boundary condition of Carter and

Merrifield (2007) prevented the reflection of baroclinic energy in all modes. The low forcing velocities ensured the velocity remained sinusoidal and linear. The simulations had a horizontal resolution of 200 m and had 300 layers in the vertical. The resulting wave field was then linearly scaled to obtain the modal distribution of the energy fluxes at other forcing amplitudes. Each numerical simulation took about 9 h on a machine with $2 \times$ Intel Xeon E5-2670, 2.6 GHz (32 CPUs effectively), and 128 GB RAM. As a comparison, the computation of 400 modes for a given stratification, forcing, and Coriolis frequencies took around 12 h on a laptop with an Intel (R) Core(TM) i7, 2.8-GHz CPU, and 4 GB RAM; once the mode shapes are computed, the Green function code takes around 20 min (on the same laptop) for each of the topographic transects.

4. Gaussian topography

To begin our investigations, we consider tidal generation by isolated Gaussian topography in the oceanographically reasonable stratification (Fig. 1a):

$$N(z) = N_0 + (N_{\text{max}} - N_0) \exp\left[-\left(\frac{z - z_c}{\sigma}\right)^2\right], \quad 0 \leq z \leq H. \quad (19)$$

We choose an ocean depth $H = 3800 \text{ m}$, a deep-ocean stratification $N_0 = 6 \times 10^{-4} \text{ rad s}^{-1}$, a maximum stratification $N_{\text{max}} = 5.48 \times 10^{-3} \text{ rad s}^{-1}$, and a pycnocline centered around $z_c = 3400 \text{ m}$ with a characteristic width $\sigma = 250 \text{ m}$. For these model studies, we choose $f = 0$, and nonzero values of f are used for our case studies in section 5; our choice of $f = 0$ has little to no impact on the overall results as its primary role is in setting the criticality of the system. The true and WKB semidiurnal (i.e., $\omega = 1.4053 \times 10^{-4} \text{ rad s}^{-1}$) mode shapes for modes 1 and 4 are presented in Figs. 1b and 1c, respectively. It is

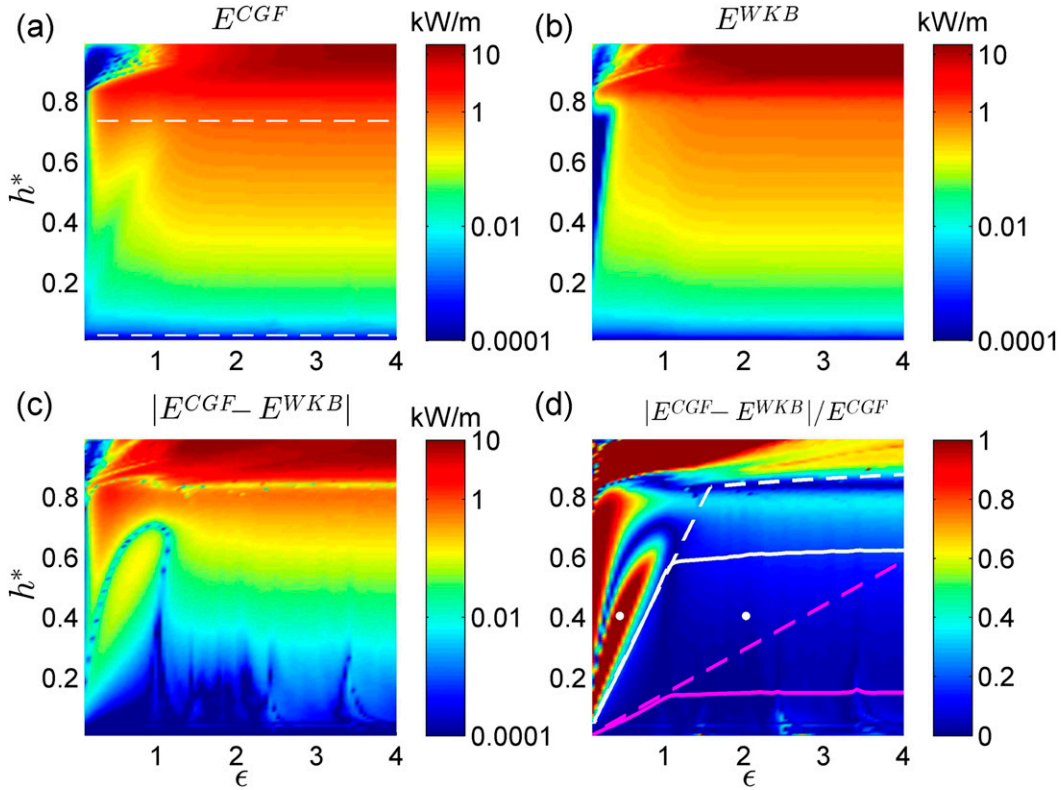


FIG. 2. The total energy flux E (kW m^{-1}) associated with the baroclinic internal tide generated (in the right or left direction) by barotropic forcing of amplitude $U = 0.02 \text{ m s}^{-1}$ as a function of the criticality ε and the height ratio h^* of the Gaussian topography defined in section 4, predicted by (a) the CGF approach and (b) the WKB approach. (c) The absolute difference between E^{CGF} and E^{WKB} and (d) the relative difference between E^{CGF} and E^{WKB} . The white dashed horizontal lines in (a) indicate the two height ratios corresponding to the data presented in Fig. 5. The white and magenta solid lines in (d) correspond to contours of $F_1^{\text{WKB}} = 0.1$ and $F_1^{\text{WKB}} + F_2^{\text{WKB}} = 0.1$, respectively. The white and magenta dashed lines in (d) correspond to contours of the ratio of the horizontal topographic scale to the horizontal mode-1 wavelength: $\sigma_G k_1 = 0.57$ and 0.16 , respectively. The white dots on the right and left sides of the figure in (d) represent topographies for which wave fields are plotted in Figs. 3 and 4, respectively.

evident that for this stratification the true mode 1 (with a horizontal wavelength of $7.95 \times 10^4 \text{ m}$) differs noticeably from its WKB counterpart (with a horizontal wavelength of $6.21 \times 10^4 \text{ m}$); the difference is relatively small, but still noticeable, for mode 4.

For an isolated Gaussian ridge,

$$h_G(x) = h_0 \exp\left(-\frac{x^2}{\sigma_G^2}\right), \quad (20)$$

we define the criticality to be $\varepsilon = \max[(dh_G/dx)/\tan\theta]$, that is, the maximum ratio of the topographic slope to the local internal wave ray slope $\{\cot\theta(z) = \sqrt{[N(z)^2 - \omega^2]/(\omega^2 - f^2)}\}$, and we define the height ratio to be $h^* = h_0/H$. Since internal tide generation for the topography described by (20) is symmetric about $x = 0$, the superscripts + and - are ignored, and we consider radiated energy flux in either direction. Figure 2a presents the variation of the radiated energy flux E as a

function of ε and h^* , obtained using the complete Green function method. For any value of h^* , E converges to a near-constant value for $\varepsilon \geq 3$, corresponding to knife-edge topography. And for all values of ε , there is a monotonic increase in the conversion rate with h^* , with a clear enhancement as the height ratio exceeds 0.8 and the topography impinges on the pycnocline.

For comparison, the WKB-predicted energy fluxes are presented in Fig. 2b, with the overall qualitative form of the results being similar to those of the complete Green function approach, presented in Fig. 2a. The WKB-predicted energy fluxes are notably different, however, and the differences between the two sets of results are highlighted in Fig. 2c, which presents the absolute value of the difference in energy flux between the two methods, and Fig. 2d, which presents the relative difference. The standout features are that the WKB method predicts energy fluxes that are $O(10) \text{ kW m}^{-1}$ higher for tall topography, and for subcritical

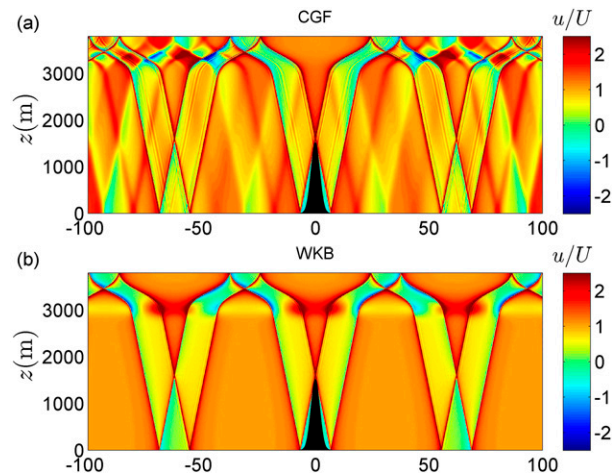


FIG. 3. The instantaneous horizontal velocity field predicted by the (a) CGF and (b) WKB approaches for the supercritical topography ($\varepsilon = 2$ and $h^* = 0.4$) indicated by the white dot on the right in Fig. 2d.

topography and topography with $h^* \geq 0.8$, the WKB predictions can be wrong by as much as 100%. For subcritical topography with large horizontal scale, Zarroug et al. (2010) have also shown that the WKB approximation in an analytical model similar to that of Bell (1975) can be unreliable in its prediction of the internal tide energy fluxes, particularly for the lower modes.

Insight into why the WKB approach is inaccurate for certain topographies is obtained by plotting the horizontal velocity fields for two different cases, namely, (i) the supercritical topography with $\varepsilon = 2$ and $h^* = 0.4$, for which the WKB approach is accurate (Fig. 3), and (ii) the subcritical topography with $\varepsilon = 0.45$ and $h^* = 0.4$, for which the WKB approach is inaccurate (Fig. 4). For the supercritical topography, the CGF and WKB wave fields have strong qualitative similarities, whereas there are notable differences (especially in the pycnocline region) for the subcritical topography case shown in Fig. 4. Upon closer inspection, we find that the wave beams emerging from the two sides of the subcritical topography are incident on the pycnocline region (and scattered back to the deeper ocean) within the horizontal extent of the topography; for the supercritical topography, however, the topography is so narrow that the waves that emerge upon reflection from the upper ocean are only incident on the floor of the constant depth ocean away from the topography. Given that the WKB approach is known to wrongly model the propagation of internal waves through nonuniform stratifications (it predicts complete transmission of waves through regions of varying stratification, which is accurate only for small enough vertical length scales in the

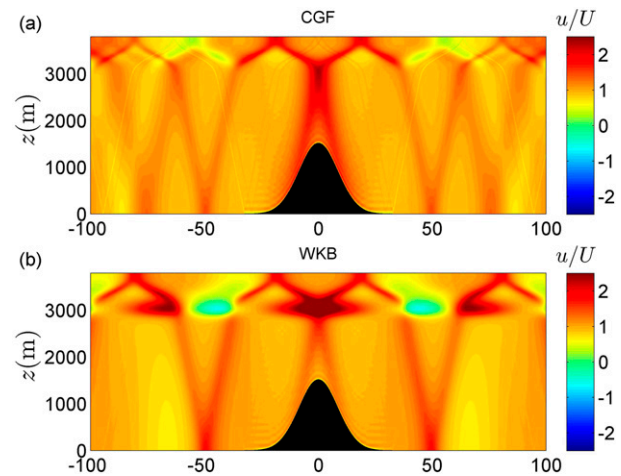


FIG. 4. As in Fig. 3, but for the subcritical topography ($\varepsilon = 0.45$ and $h^* = 0.4$) indicated by the white dot on the left in Fig. 2d.

waves) and the modal representation of the generated wave field formally applies in regions beyond the topography, these results suggest that the topographic width relative to the horizontal scale of the generated internal waves is a significant parameter that affects the accuracy of the WKB approach. This is furthermore consistent with the results of Zarroug et al. (2010) for subcritical topography that the WKB approach is susceptible to larger errors for wider topographies.

To validate our findings, Fig. 5a presents comparisons between the two analytical approaches and the results of numerical simulations for E_1 and E_4 for $h^* = 0.73$ and varying criticality. There is excellent agreement between the numerical results and the theoretical predictions using the complete Green function approach. The WKB approach underpredicts E_1 for subcritical regimes and overpredicts it for supercritical regimes and furthermore somewhat underpredicts E_4 for supercritical regimes. As shown in Fig. 5b, for $h^* = 0.025$, the complete Green function prediction for E_1 is in close agreement with the numerical simulations for all criticalities. In the subcritical regime, the WKB method overpredicts E_1 by more than a 100%, which is somewhat in contrast to the results of Zarroug et al. (2010) where the WKB approach underpredicted energy fluxes for small-amplitude, subcritical topography. Upon further analysis of our results, we find that for a fixed h^* , the WKB method underpredicts E_1 for $0 < \varepsilon < \varepsilon^*$ and then overpredicts E_1 for $\varepsilon > \varepsilon^*$. The threshold criticality ε^* is larger for larger h^* ; while the studies of Zarroug et al. (2010) were in the $\varepsilon < \varepsilon^*$ regime, the plot in Fig. 5b shows only the $\varepsilon > \varepsilon^*$ range. For E_4 , the results from all three approaches are quantitatively very similar for all criticalities except $\varepsilon = 0.1$, for which the results from numerical simulations contain significant spatial variations

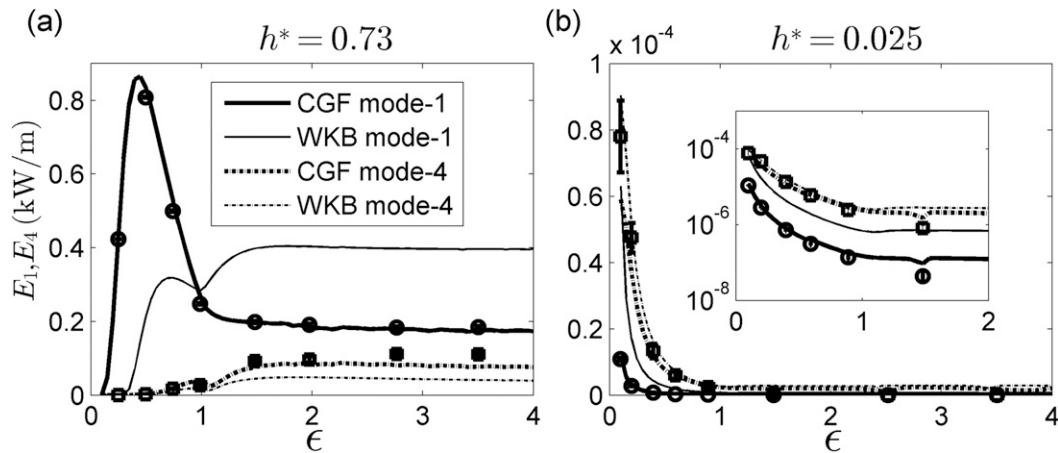


FIG. 5. The terms E_1 and E_4 as a function of ϵ for (a) $h^* = 0.73$ and (b) $h^* = 0.025$. Both the plots correspond to a barotropic forcing amplitude of $U = 0.02 \text{ m s}^{-1}$. Thick and thin lines correspond to the CGF and WKB solutions, respectively. Solid and dashed lines correspond to E_1 and E_4 , respectively. Circles (E_1) and squares (E_4) correspond to results from numerical simulations. The data in (b) are replotted in its inset with a log scale on the y axis to bring out the variations more clearly.

in the mode-4 energy flux, suggesting that they may not be in the linear regime. Moreover, for small-amplitude, small criticality topography, it may be required to use a larger total number of modes for the complete Green function solution to converge.

Having established the validity of the complete Green function approach in Fig. 5, we proceed to identify regions in the ϵ - h^* plane where the WKB may be considered accurate. Since the characteristic vertical wavelength of a mode decreases as the mode number increases, the discrepancy between a true mode shape and its corresponding WKB mode shape monotonically decreases with the increasing mode number. One therefore expects the WKB approach to be accurate in scenarios for which the generated internal tide energy is predominantly put into the higher modes. To test this hypothesis, we plot the contour (shown as white solid line) corresponding to $F_1^{\text{WKB}} = E_1^{\text{WKB}}/E^{\text{WKB}} = 0.1$ in Fig. 2d, and indeed it is evident that the $F_1^{\text{WKB}} = 0.1$ contour delineates regions of large and small relative errors in E^{WKB} . We furthermore plot the contour (shown as a magenta solid line) corresponding to $(F_1^{\text{WKB}} + F_2^{\text{WKB}}) = (E_1^{\text{WKB}} + E_2^{\text{WKB}})/E^{\text{WKB}} = 0.1$ in Fig. 2d, which further reveals that when there are small fractional energy fluxes in both modes 1 and 2 then the relative errors in E^{WKB} become even smaller. Insight into the form of these error plots is provided by the results of Zarroug et al. (2010), who find that in regards to the WKB approximation the crucial aspect of topography is its horizontal length scale relative to the horizontal length scale of the internal waves since that determines the depth region over which the stratification is sampled. We therefore plot lines of constant σ_G

(the white and magenta dashed lines in Fig. 2d correspond to $\sigma_G k_1 = 0.57$ and 0.16 , respectively) and observe that lines of constant ridge width indeed seem to follow the orientation of the error features in Fig. 2d for subcritical topography. The slope of the white dashed line abruptly changes at around $\epsilon \approx 1.6$ as the criticality is defined as the maximum ratio of the local topographic slope to the local internal wave ray slope. As the topography impinges on the pycnocline, the value of this maximum ratio changes significantly with the height ratio for a fixed value of $\sigma_G k_1$ due to the much shallower internal wave ray slopes in the pycnocline.

An overall summary of the important fundamental scenario of Gaussian topography in an oceanographically reasonable, nonuniform stratification is that while the complete Green function approach consistently agrees with the results of the full numerical simulations, thus validating the method, WKB predictions for the overall energy flux are really only accurate for strongly supercritical topographies of modest-to-small height ratio. Significantly, the WKB approach is inaccurate for very subcritical topography with even small height ratios. An alternate but equivalent summary is that WKB predictions for the overall energy flux are accurate only if the topographic length scale is less than half of the horizontal scale of the first mode, and the height ratio is modest to small.

5. Realistic topography

The capability of the Green function method to determine internal tide generation for realistic oceanic scenarios was investigated by Echeverri and Peacock

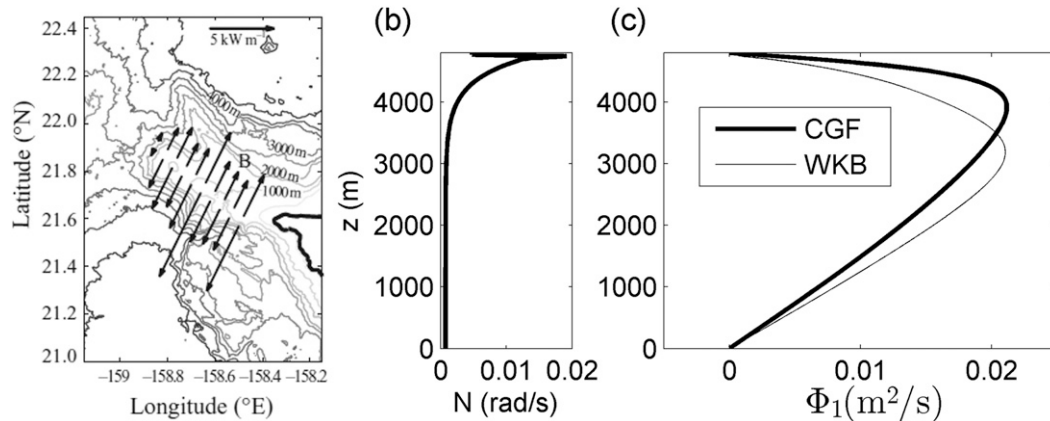


FIG. 6. (a) A contour plot of the depth of the topography (measured from the sea surface) at the Kaena Ridge. Investigations are performed for the 10 transects shown using double-headed arrows; the size of the arrows is directly proportional to the total, generated, internal tide energy flux calculated using the WKB approximation (Echeverri and Peacock 2010). (b) A typical stratification for the region shown in (a). (c) Mode-1 streamfunction $\Phi_1(z)$, as obtained by solving (6) numerically (thick line) and the WKB approach (thin line), for the stratification presented in (b), with $\omega = 1.4053 \times 10^{-4} \text{ rad s}^{-1}$ (M_2) and $f = 5 \times 10^{-5} \text{ rad s}^{-1}$. The term Φ_1 is normalized so that $\int_0^H \Phi_1^2 dz = 1$. Image in (a) reproduced from Echeverri and Peacock (2010).

(2010) in the limit of the WKB approximation. In this section, we similarly use the complete Green function method to investigate internal tide generation along 2D transects across the Kaena Ridge near the Hawaiian Islands and the Wyville Thomson Ridge near the Faroe–Shetland Channel; these two scenarios were chosen because they present quite different configurations in terms of the background stratification profile and the topographic shapes. The predictions are compared with those of WKB theory and the results of our numerical model.

a. Kaena Ridge

The topography and stratification considered in this section are those used in section 4.1 in Echeverri and Peacock (2010). Specifically, as shown in Fig. 6a, we consider 10 evenly spaced 140-km-long transects across the Kaena Ridge. The stratification profile $N(z)$, as shown in Fig. 6b, comprises a pycnocline, where N attains a maximum value of $0.0191 \text{ rad s}^{-1}$ at 55 m below the sea surface in an ocean of total depth of around 4800 m (the specific value depending weakly on the transect number) and a deep-ocean stratification of $7.63 \times 10^{-4} \text{ rad s}^{-1}$. We consider semidiurnal forcing ($\omega = 1.4053 \times 10^{-4} \text{ rad s}^{-1}$), and the local Coriolis parameter is $f = 5 \times 10^{-5} \text{ rad s}^{-1}$. Figure 6c shows a discernable difference between the mode-1 shapes computed with and without the WKB approximation.

Figure 7a presents the complete Green function model prediction for a snapshot of the total horizontal velocity field for 1 of the 10 transects' sections we consider at the Kaena Ridge. The corresponding wave field

determined by numerical simulations is presented in Fig. 7b. There is a remarkable similarity between the results of theory and numerics, with wave beams emanating from the same locations on the topography in both the plots. In the numerical model, the wavebeams become diffuse as they radiate away from the topography because of the numerical dissipation, whereas the inviscid wavebeams in the analytic solution remain

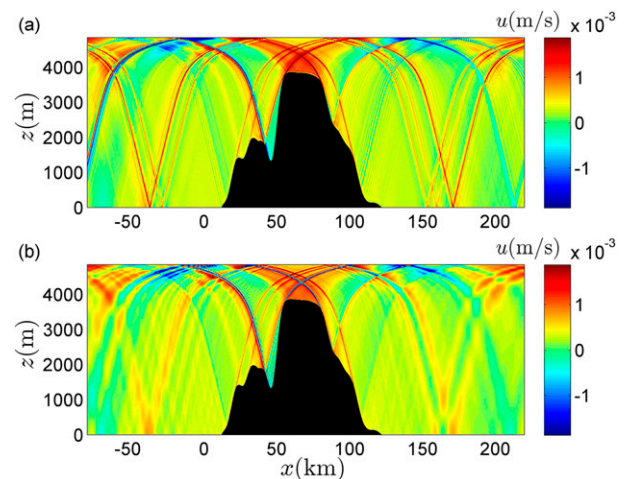


FIG. 7. A snapshot of the total horizontal velocity field u at 1 of the 10 topographic sections of the Kaena Ridge predicted by (a) the complete Green function method and (b) numerical simulations. Both the wave fields correspond to a (linear) barotropic forcing amplitude of $2.5 \times 10^{-4} \text{ m s}^{-1}$ for the horizontal velocity; x is the distance measured along the transect under consideration. The northeast and southwest directions correspond to $x > 0$ and $x < 0$, respectively.

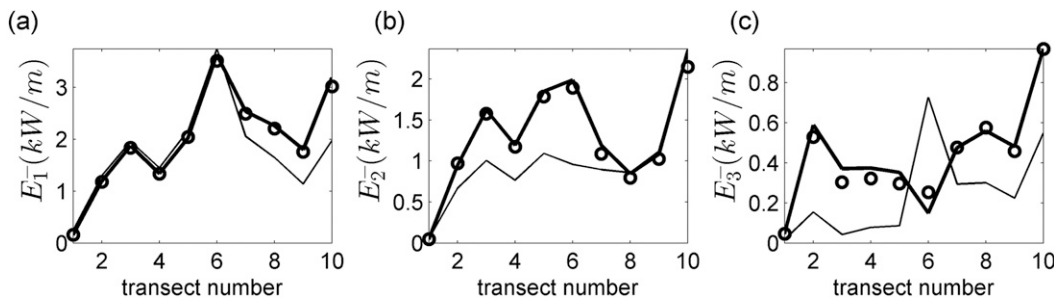


FIG. 8. Energy fluxes in the southwestward-propagating internal tides generated by barotropic forcing of amplitude $U = 0.02 \text{ m s}^{-1}$ at the Kaena Ridge. Plotted in the various figures are the energy fluxes in the first three modes: (a) E_1^- , (b) E_2^- , and (c) E_3^- . Thick and thin solid lines correspond to the complete Green function and WKB methods, respectively, and circles denote results from the numerical simulations.

indefinitely sharp. A similar level of agreement was obtained for the other nine cross sections as well.

As a more quantitative comparison between the results of the theory without and with the WKB approximation, and with the predictions of the numerical model, Figs. 8a–c present the variation of the internal tide energy flux in the first three modes in the southwest direction across the 10 topographic transects. We observe large differences between the theoretical model without and with the WKB approximation, and there is generally excellent quantitative agreement between the results of the complete Green function method and the numerical simulations. The mean, standard deviation, and maximum of the relative error (with respect to the complete Green function method) of the WKB predictions across all 10 transects for E_1^- are 20.7%, 17.6%, and 54.4%, respectively; for E_2^- and E_3^- , they are 23.6%, 18.6%, and 51.8% and 94.7%, 103.6%, and 385.7%, respectively. In contrast, across the 10 transects, the mean relative differences between the complete Green

function approach and the numerical model are 2%, 4.6%, and 13.7% for E_1^- , E_2^- , and E_3^- , respectively. It is interesting to note that although WKB is considered to be most accurate for higher modes, it is for the higher modes that there is the greatest fractional error. This is because the modal amplitudes are not calculated independently but are coupled through the bottom boundary condition, and so an error in mode 1 can significantly impact the determination of higher modes.

b. Wyville Thomson Ridge

The Wyville Thomson Ridge is an ~140-km-long topographic feature located at the southwestern end of the Faroe–Shetland Channel. A contour plot of a roughly 2° latitude by 2.5° longitude section of this ridge system, centered near 60°N and 7.5°W , is presented in Fig. 9a. Field observations reveal strong internal tides and subsequent mixing in the region, with corresponding numerical modeling attributing a part of the source of these internal tides to generation at the Wyville Thomson

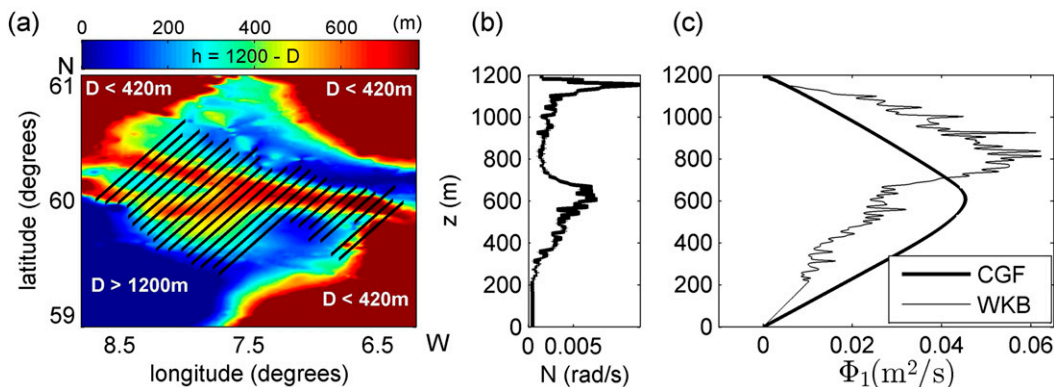


FIG. 9. (a) A contour plot of the topography at the Wyville Thomson Ridge (D is the depth of the topography measured from the sea surface). Investigations are performed for the 25 equispaced transects shown in black. (b) A typical stratification for the region shown in (a). (c) Mode-1 streamfunction $\Phi_1(z)$, as obtained by solving (6) numerically (thick line) and the WKB approach (thin line), for the stratification presented in (b), with $\omega = 1.4053 \times 10^{-4} \text{ rad s}^{-1}$ (M_2) and $f = 1.26 \times 10^{-4} \text{ rad s}^{-1}$ (60°N). The term Φ_1 is normalized so that $\int_0^H \Phi_1^2 dz = 1$.

Ridge (Hall et al. 2011). Figure 9b presents a typical stratification, comprising two pycnoclines: a relatively strong one at 100-m depth and a relatively weak one at 600-m depth, beneath a nearly constant stratification of $N = 4.59 \times 10^{-4} \text{ rad s}^{-1}$. For this stratification, and using $\omega = 1.4053 \times 10^{-4} \text{ rad s}^{-1}$ (M_2) and $f = 1.26 \times 10^{-4} \text{ rad s}^{-1}$ (corresponding to a latitude of 60°N), plots of the vertical structure of mode 1 (Φ_1) based on (6) and the WKB approach are presented in Fig. 9c. The WKB mode 1, which contains small-scale noise similar to those in $N(z)$, is notably different from Φ_1 . We choose to work with the noisy $N(z)$ profile (instead of smoothening it to retain only the large-scale features) so as to demonstrate the robustness and accuracy of the complete Green function approach even in the presence of small-scale features in $N(z)$. We note that stratification profiles with a double pycnocline structure are found in other parts of the ocean too, the Arctic Circle (Pinkel 2005) and the Bay of Bengal (Sengupta et al. 2006), for example.

We consider 25 different two-dimensional topographic cross sections, indicated in Fig. 9a, and the barotropic tidal forcing is assumed to be in the northeast/southwest direction with a magnitude of 0.104 m s^{-1} , corresponding to an amplitude of $104 \text{ m}^2 \text{ s}^{-1}$ for the volume flow per unit width of the barotropic tide in a 1000-m deep ocean (Sherwin 1991). Topography reaches within 300–500 m of the ocean surface in some locations, and outside this domain topography is assumed to smoothly descend to a constant ocean depth of 900–1200 m, the specific value depending on the cross section. The start and the end points for every cross section are chosen such that $z > 0$ throughout, as the analysis requires $z = 0$ on either side of the topography and $z \geq 0$ everywhere in the topographic domain.

Figure 10a presents a snapshot of the theoretical prediction (based on the complete Green function approach) of the horizontal velocity field for one of the 25

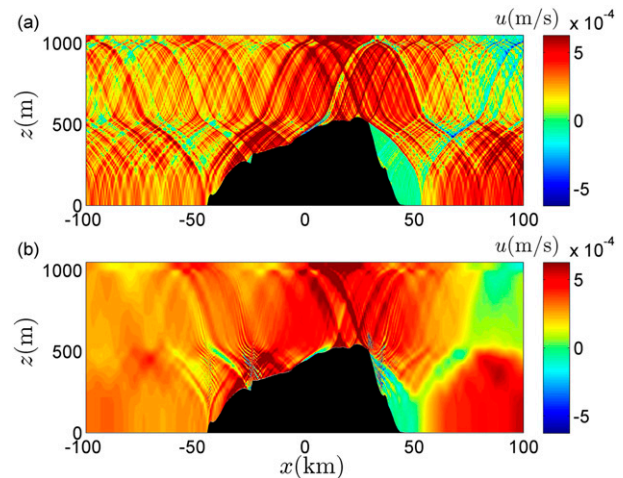


FIG. 10. As in Fig. 7, but at one of the 25 topographic transects of the Wyville Thomson Ridge.

topographic sections; the corresponding wave field determined by the numerical model is presented in Fig. 10b. The resulting wave field is highly complex, resulting from multiple reflections that occur where the stratification changes significantly, but there is nevertheless striking qualitative agreement between the two wave fields. As a more quantitative comparison, the variations of the northeastward-propagating energy flux for the first three modes are plotted for the 25 transects in Figs. 11a–c. There are very large differences between the complete Green function and WKB approaches, especially for modes 2 and 3, and again there is excellent quantitative agreement in E_1^+ and E_2^+ between the complete Green function model and numerical simulations. The mean, standard deviation, and maximum of the WKB errors in E_1^+ , E_2^+ , and E_3^+ are 38.1%, 115.7%, and 9639.1%, 17.9%, 149.8%, and 40036.8%, and 83.8%, 546.2%, and 201 615.5%, respectively. As a reality check,

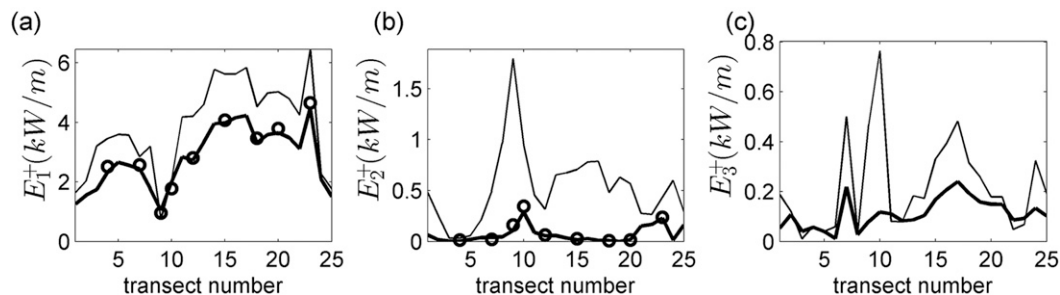


FIG. 11. Energy fluxes in the northeastward-propagating internal tides generated at the Wyville Thomson Ridge. Plotted in the various figures are the energy fluxes in the first three modes: (a) E_1^+ , (b) E_2^+ , and (c) E_3^+ . Thick and thin solid lines correspond to the complete Green function and WKB methods, respectively, whereas the circles denote results from the numerical simulations. The numerical simulations were not run for a long enough duration for the energy flux in mode 3 to achieve steady state; it is noteworthy that the mode-3 energy flux at the Faroe–Shetland Channel travels around 6 times slower horizontally than at the Kaena Ridge discussed in section 5a.

the mean, standard deviation, and maximum of the energy flux E^+ in the complete Green function–based predictions (considering all 25 transects) are 3.27, 1.02, and 5.28 kW m^{-1} , respectively. This is consistent with the 3D estimates of Hall et al. (2011), who determined fluxes to be $>5 \text{ kW m}^{-1}$ on the northern flank of the Wyville Thomson Ridge.

6. Conclusions

The Green function method, which to date has been used to study internal tide generation by barotropic flow over topography in constant stratifications and nonuniform stratifications in the limit of the WKB approximation, has been advanced to account for fully nonuniform stratifications. To validate the method and to test the inaccuracies of WKB approximate solutions, tidal generation was first studied for idealized isolated Gaussian topography in a realistic ocean stratification. Consistently excellent agreement was obtained between the complete Green function solution and the results of numerical simulations. The WKB approach, however, was found to give substantial errors in the subcritical regime even for small height ratios, and as the height ratio becomes larger and the topography starts to impinge on the pycnocline, there are furthermore large errors for both subcritical and supercritical scenarios.

Studies were then performed for realistic ocean scenarios using cross-sectional profiles of the Kaena and Wyville Thomson Ridges. Again, in all cases, the solutions of the complete Green function approach and numerical simulations were in excellent agreement. The relative errors of the WKB approach for the Kaena Ridge, however, were on average around 25% for the energy fluxes in the first two modes, although with much larger errors for some specific cross sections. For the Wyville Thomson Ridge, which has a more complex double pycnocline stratification, the WKB approach was highly inaccurate; the mean total generated energy flux based on the WKB approach is 10.77 kW m^{-1} , whereas the value based on the complete Green function approach is 5.37 kW m^{-1} , thus resulting in a 100% error for the WKB approach. As with the Kaena Ridge scenario, the WKB errors in the energy fluxes in the individual modes are much larger.

We conclude that in order to reasonably estimate the energy flux in individual modes of the internal tide generated by barotropic tidal flow over ocean ridges it is necessary to use the complete Green function approach developed in this paper and not to resort to the WKB approximate solution. We have thoroughly investigated whether there are conditions under which one can reliably use the WKB approximation for idealized

Gaussian topography and for realistic topography. Our conclusion is that WKB predictions can be quite sensitive to errors in the mode shapes, and given that the computational demands of the complete Green function method are significantly less than those of the numerical simulations (see section 3 for a quantitative comparison), the former should be used at all times, safe in the knowledge that this approach has now been thoroughly validated by direct comparison with numerical simulations. As a follow-up study, it would be intriguing to perform global estimates of internal tide generation along the lines of Falahat et al. (2014) using the complete Green function approach, albeit in the two-dimensional limit but with the capability to model supercritical topographies also.

Finally, we note that a variation of the approach that we present can be used to study topographic scattering of low-mode internal tides, a mechanism believed to be important to identify and quantify the processes by which internal waves dissipate in the ocean. The results of such a study appear in Mathur et al. (2014). With that study and the present study in hand, linear, two-dimensional, internal tide generation and scattering by deep-ocean topography are now quite well considered, although scenarios such as the impact of steady flow and nonlinearities (Lamb 2004) still need to be fully addressed. Moving forward, attention also needs to be directed toward developing reliable analytical methods to study internal tide generation and scattering by three-dimensional topography (e.g., Munroe and Lamb 2005; King et al. 2010).

Acknowledgments. MM thanks the Ministry of Earth Sciences, Government of India for financial support under the Monsoon Mission Grant MM/2014/IND-002. TP acknowledges funding from National Science Foundation Grants OCE 0645529 and OCE1129757. GSC acknowledges funding from the National Science Foundation Grant OCE 0825266. The comments from the reviewers, which have helped improve the manuscript, are also acknowledged.

REFERENCES

- Baines, P. G., 1982: On internal tide generation models. *Deep-Sea Res.*, **29A**, 307–338, doi:10.1016/0198-0149(82)90098-X.
- Balmforth, N. J., and T. Peacock, 2009: Tidal conversion by supercritical topography. *J. Phys. Oceanogr.*, **39**, 1965–1974, doi:10.1175/2009JPO4057.1.
- , G. R. Ierley, and W. R. Young, 2002: Tidal conversion by subcritical topography. *J. Phys. Oceanogr.*, **32**, 2900–2914, doi:10.1175/1520-0485(2002)032<2900:TCBST>2.0.CO;2.
- Bell, T. H., 1975: Topographically generated internal waves in the open ocean. *J. Geophys. Res.*, **80**, 320–327, doi:10.1029/JC080i003p00320.

- Blumberg, A. F., and G. L. Mellor, 1987: A description of a three-dimensional coastal ocean circulation model. *Three-Dimensional Coastal Ocean Models*, Coastal Estuarine Sci., Vol. 4, Amer. Geophys. Union, 1–16.
- Carter, G. S., and M. A. Merrifield, 2007: Open boundary conditions for regional tidal simulations. *Ocean Modell.*, **18**, 194–209, doi:10.1016/j.ocemod.2007.04.003.
- Echeverri, P., and T. Peacock, 2010: Internal tide generation by arbitrary two-dimensional topography. *J. Fluid Mech.*, **659**, 247–266, doi:10.1017/S0022112010002417.
- Falahat, S., J. Nycander, F. Roquet, and M. Zarroug, 2014: Global calculation of tidal energy conversion into vertical normal modes. *J. Phys. Oceanogr.*, **44**, 3225–3244, doi:10.1175/JPO-D-14-0002.1.
- Flather, R. A., 1976: A tidal model of the north-west European continental shelf. *Mem. Soc. Roy. Sci. Liege*, **6**, 141–164.
- Hall, R. A., J. M. Huthnance, and R. G. Williams, 2011: Internal tides, nonlinear internal wave trains, and mixing in the Faroe-Shetland Channel. *J. Geophys. Res.*, **116**, C03008, doi:10.1029/2010JC006213.
- Holloway, P. E., and M. A. Merrifield, 1999: Internal tide generation by seamounts, ridges, and islands. *J. Geophys. Res.*, **104**, 25 937–25 951, doi:10.1029/1999JC900207.
- King, B., H. P. Zhang, and H. L. Swinney, 2010: Tidal flow over three-dimensional topography generates out-of-forcing-plane harmonics. *Geophys. Res. Lett.*, **37**, L14606, doi:10.1029/2010GL043221.
- Lamb, K. G., 2004: Nonlinear interaction among internal wave beams generated by tidal flow over supercritical topography. *Geophys. Res. Lett.*, **31**, L09313, doi:10.1029/2003GL019393.
- Llewellyn-Smith, S. G., and W. R. Young, 2002: Conversion of the barotropic tide. *J. Phys. Oceanogr.*, **32**, 1554–1566, doi:10.1175/1520-0485(2002)032<1554:COTBT>2.0.CO;2.
- , and —, 2003: Tidal conversion at a very steep ridge. *J. Fluid Mech.*, **495**, 175–191, doi:10.1017/S0022112003006098.
- Mathur, M., G. S. Carter, and T. Peacock, 2014: Topographic scattering of the low mode internal tide in the deep ocean. *J. Geophys. Res. Oceans*, **119**, 2165–2182, doi:10.1002/2013JC009152.
- Mellor, G. L., and T. Yamada, 1982: Development of a turbulence closure model for geophysical fluid problems. *Rev. Geophys.*, **20**, 851–875, doi:10.1029/RG020i004p00851.
- Munk, W., and C. Wunsch, 1998: Abyssal recipes II: Energetics of tidal and wind mixing. *Deep-Sea Res.*, **45**, 1977–2010, doi:10.1016/S0967-0637(98)00070-3.
- Munroe, J. R., and K. G. Lamb, 2005: Topographic amplitude dependence of internal wave generation by tidal forcing over idealized three-dimensional topography. *J. Geophys. Res.*, **110**, C02001, doi:10.1029/2004JC002537.
- Pétrélis, F., S. G. Llewellyn-Smith, and W. R. Young, 2006: Tidal conversion at a submarine ridge. *J. Phys. Oceanogr.*, **36**, 1053–1071, doi:10.1175/JPO2879.1.
- Pinkel, R., 2005: Near-inertial wave propagation in the western Arctic. *J. Phys. Oceanogr.*, **35**, 645–665, doi:10.1175/JPO2715.1.
- Robinson, R. M., 1969: The effects of a vertical barrier on internal waves. *Deep-Sea Res. Oceanogr. Abstr.*, **16**, 421–429, doi:10.1016/0011-7471(69)90030-8.
- Sengupta, D., G. N. B. Raj, and S. S. C. Shenoi, 2006: Surface freshwater from Bay of Bengal runoff and Indonesian Throughflow in the tropical Indian Ocean. *Geophys. Res. Lett.*, **33**, L22609, doi:10.1029/2006GL027573.
- Sherwin, T. J., 1991: Evidence of a deep internal tide in the Faeroe-Shetland Channel. *Tidal Hydrodynamics*, B. B. Parker, Ed., 469–488.
- Smagorinsky, J., 1963: General circulation experiments with the primitive equations. I. The basic experiment. *Mon. Wea. Rev.*, **91**, 99–164, doi:10.1175/1520-0493(1963)091<0099:GCEWTP>2.3.CO;2.
- Zarroug, M., J. Nycander, and K. Döös, 2010: Energetics of tidally generated internal waves for nonuniform stratification. *Tellus*, **62A**, 71–79, doi:10.1111/j.1600-0870.2009.00415.x.